JOURNAL OF SPACECRAFT AND ROCKETS
Vol. 34, No. 1, January–February 1997

# Monte Carlo Modeling and Analysis of Pressure Sensor Measurements During Suborbital Flight

N. A. Gatsonis,* and E. P. Maynard†
*Worcester Polytechnic Institute, Worcester, Massachusetts 01609*
R. E. Erlandson‡
*Johns Hopkins University, Applied Physics Laboratory, Laurel, Maryland 20723*

**The response of an ionization pressure sensor onboard a rotating suborbital spacecraft is investigated with data analysis and direct simulation Monte Carlo computations. The sensor housed in a chamber was connected to the spacecraft surface with a tube and recorded asymmetric ram-wake pressure pulses during the nonthrusting period of the mission. Three-dimensional Monte Carlo computations of the external and internal flows are performed using a domain that includes the spacecraft and the pressure apparatus. Freestream parameters correspond to altitudes between 130 and 275 km. The flux and composition at the sensor tube entrance is found to depend on the tube's orientation with the freestream during the spacecraft rotation. The predicted external pressure pulse differs from measurements because of internal flow effects. The flow structure is three-dimensional at the tube entry region and becomes axisymmetric a few tube diameters inside. The temperature, density, and surface pressure distributions inside the tube and chamber are found to depend on the tube orientation with the freestream and demonstrate the coupling between external and internal flows. The predicted pressure pulse is in good qualitative agreement with measurements. Differences in magnitude are attributed to the uncertainty in the freestream parameters.**

## Nomenclature

(A)–(H) = tube position during a revolution
$D_t$ = tube diameter, m
$L^t$ = tube length, m
$n_\infty$ = freestream number density, $m^{-3}$
$o$ = angle between freestream velocity and $Y$ axis, deg
$R_i$ = pressure pulse $i$, $i = 1, 17$
$T_\infty$ = freestream temperature, $K$
$V_\infty$ = freestream velocity, m/s
$X, Y, Z$ = Environmental Monitor Package spacecraft axis
$\lambda_\infty$ = mean-free path, m
$\theta$ = polar angle of tube entrance measured from the freestream velocity

## Introduction

MEASUREMENTS of environmental parameters around spacecraft often are obtained with instruments housed inside the vehicle and connected to the surface through openings or tubes (e.g., neutral and ion mass spectrometers, pressure gauges). The incident flux and composition at the entrance to such an opening are related to the external flowfield; the measurements taken inside the apparatus are affected by the internal flow as well. In addition, spacecraft perturb the ambient environment and introduce additional components and disturbances due to outgassing, thruster firings, or other gas releases. The interpretation of flight data in such cases is difficult because of the compound effects of the external and internal flowfields.

The problems of external rarefied flows over bodies, as well as those inside tubes, have received considerable attention independently over the years. The external flowfield over a body in a rarefied flow can be analyzed with the direct simulation Monte Carlo (DSMC) technique, which employs a large number of computational particles to simulate the real gas particles.[1] The DSMC method is capable of capturing important nonequilibrium effects, as has been shown in the numerous studies of rarefied flows over bodies.[2,3] Recent computational advances allow the DSMC modeling of complex three-dimensional geometries as well.[4] The problem of flows in the near and free molecular regimes through tubes also has been studied analytically and computationally for many years because of its importance in many technical applications.[5–7] Most of the previous efforts considered flows of single gases in tubes connected to either large reservoirs or to vacuum and were based on approximations that limit their applicability to real spacecraft instruments. Moss and Bird[8] used external-flow axisymmetric DSMC predictions as inputs to the internal DSMC calculations to investigate the response of a mass spectrometer on the Shuttle.

In this study we are concerned with the analysis of pressure measurements recorded with an ionization pressure sensor onboard the Environmental Monitor Package (EMP) suborbital vehicle. The pressure sensor was housed in a chamber inside the spacecraft and was connected to the outside with a 0.1-m length and 0.022-m-diam tube located off the axis of the conical EMP spacecraft. Pressure measurements were obtained while the attitude-control thrusters of the spacecraft were firing, as well as during quiet thruster periods. Data analysis revealed pressure spikes that coincide with the firings, as well as plume wraparound and freestream plume interactions. During the quiet thruster period, from an altitude of 560 km and until reentry at 130 km, the pressure sensor recorded pulses characteristic of the ram-wake rotation of the EMP spacecraft. The most distinct characteristic of the pressure pulses was their asymmetry with respect to their peak position.

To investigate the response of the EMP pressure sensor and its connecting tube to the incoming rarefied flow, the quiet thruster ram-wake period is examined. The objectives are to analyze the data and perform numerical simulations using the DSMC method, examining both external and internal flowfield effects on the pressure sensor.

A three-dimensional DSMC code is used to analyze the flowfield over the entire EMP spacecraft with freestream conditions appropriate for altitudes between 130 and 275 km and a freestream velocity of 6.5 km/s. The external-flow DSMC simulations are performed to compare predictions of the pressure incident to the sensor tube entrance with internal measurements. In addition, external simulations investigate the three-dimensional and nonequilibrium character of the flow at the tube entry region during a complete spacecraft

Received April 4, 1996; revision received Oct. 15, 1996; accepted for publication Oct. 17, 1996. 

*Assistant Professor, Mechanical Engineering Department, 100 Institute Road. Member AIAA.
†Graduate Research Assistant, Mechanical Engineering Department, 100 Institute Road.
‡Senior Professional Staff, Johns Hopkins Road. Member AIAA.

revolution. Subsequent DSMC simulations are focused on the internal flowfield of the EMP pressure apparatus itself. A large computational domain is utilized that includes the sensor tube, the chamber, and the EMP surface, to account for the coupling of the external and internal flows. The tube and chamber density, temperature, and surface pressure are investigated during the EMP revolution. The DSMC pressure predictions are compared with measurements and theory.

## Experiment Description and Data Analysis

The EMP payload was part of an experiment conducted by the Applied Physics Laboratory and contained a suite of instruments designed to measure the induced environment around a suborbital spacecraft. An engineering view of the EMP spacecraft is shown in Fig. 1. The approximate altitude and speed of the spacecraft as a function of time is shown in Fig. 2. This profile is based on limited trajectory data available for the EMP mission. The spacecraft used the attitude-control system shown in Fig. 3 after its separation from the postboost vehicle. There were eight $N_2$ cold gas thrusters:

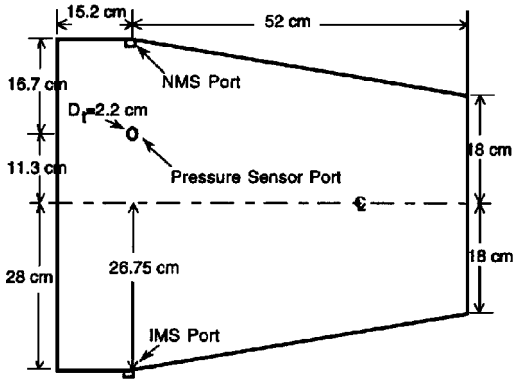


**Fig. 1 EMP spacecraft geometry and instrument location.**

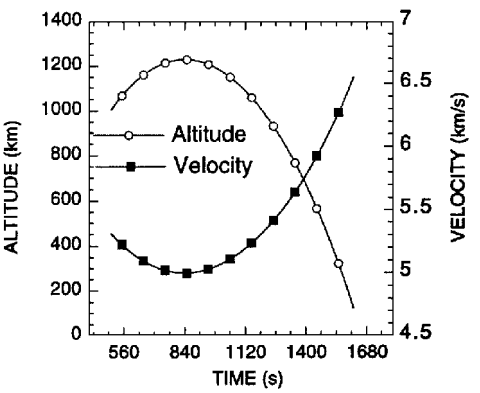


**Fig. 2 Approximate EMP altitude and speed during the mission.**

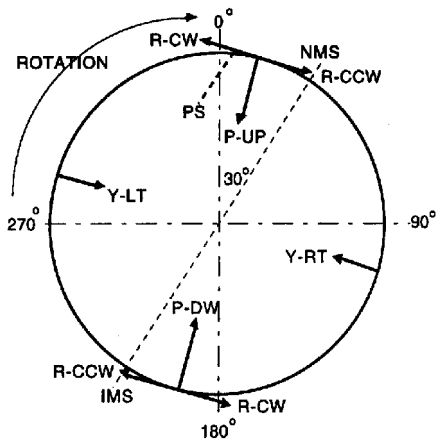


**Fig. 3 Attitude-control thruster location (base of EMP looking forward).**

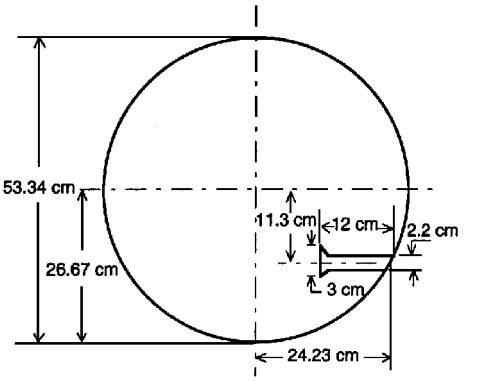


**Fig. 4 EMP view of pressure-sensor plane (looking aft).**

pitch-up, pitch-down, yaw-right, yaw-left, two roll-clockwise (roll CW), and two roll-counterclockwise (roll-CWW). The pitch and yaw thrusters delivered 1.245 N of thrust; the roll thruster delivered 3.278 N with cold gas impulses that lasted 0.03 s each.

The neutral gas pressure was monitored by a cold cathode ionization sensor. The operating range of the sensor was $4 \times 10^{-5}$ Pa to 0.1333 Pa, and the absolute values are expected to be correct to within 15%. The sensor was capable of measurements at 100 Hz, although in this experiment the pressure was sampled at 16 Hz. The pressure sensor itself was housed inside the spacecraft and was connected to the entrance hole on the surface by a tube with length $L_t = 0.1$ m and diameter $D_t = 0.022$ m. The pressure tube was located approximately 0.11 m off the axis at a plane 0.15 m from the base of the spacecraft. The geometry at the plane of the pressure-sensor is shown in Fig. 4.

The pressure recorded by the sensor for the entire flight from 500 to 1630 s is shown in Fig. 5. This data set can be clearly divided into two periods. The first period ends at approximately 1420 s and exhibits large pressure spikes. At approximately 1420 s, the $N_2$ gas was depleted and the pressure spikes disappear. The second period, starting at 1450 s, covers a quiet thruster period until reentry at approximately 1630 s. At 1450 s, while the spacecraft was at approximately 560 km, periodic pulses appear related to ram-wake effects, as shown in Fig. 5. These pressure pulses increase in amplitude up to reentry at an altitude of approximately 130 km. The entire pressure envelope shown in Fig. 5 is superimposed on a background pressure that decreases with time. This background pressure is shown also in Fig. 5 and is associated with the outgassing of the external surfaces of the spacecraft, as well as the internal surfaces of the pressure-sensor chamber and tube itself.

### Thruster-Firings Period

A typical pressure profile during thruster firings is shown in Fig. 6 for the period between 550 and 575 s. The pressure spikes and the thruster firings coincide within the temporal resolution of the sampling, as Fig. 6 shows. From the data, it is evident that although the thrusters did not have a direct line of sight with the pressure sensor, they caused instantaneous pressure increases. Analysis of individual thruster effects suggests that thrusters of the same thrust levels did not produce similar pressure effects. For example, the roll-CWW thruster produced almost an order of magnitude larger pressure amplitudes than the roll-CW. In contrast, differences between the yaw thrusters are small. All of the above suggests that significant plume wraparound and plume-surface interactions are in effect. The thruster firing period will be the subject of a future investigation.

### Ram-Wake Period

The pressure data between 1450 and 1630 s are shown in detail in Figs. 7a and 7b. There are 17 revolutions of the spacecraft during this period and an equal number of distinct pressure pulses designated by $R_i$. The pressure amplitude increases from $2 \times 10^{-4}$ Pa for the first revolution $R_1$ to almost 0.3 Pa during the last revolution $R_{17}$. The period of these pulses has been determined to be 9.25 s.

The geometry of the EMP spacecraft, the direction of the EMP rotation, the incoming flow, and the entrance of the tube are shown in Fig. 8. The axis of the EMP spacecraft is taken to be aligned with

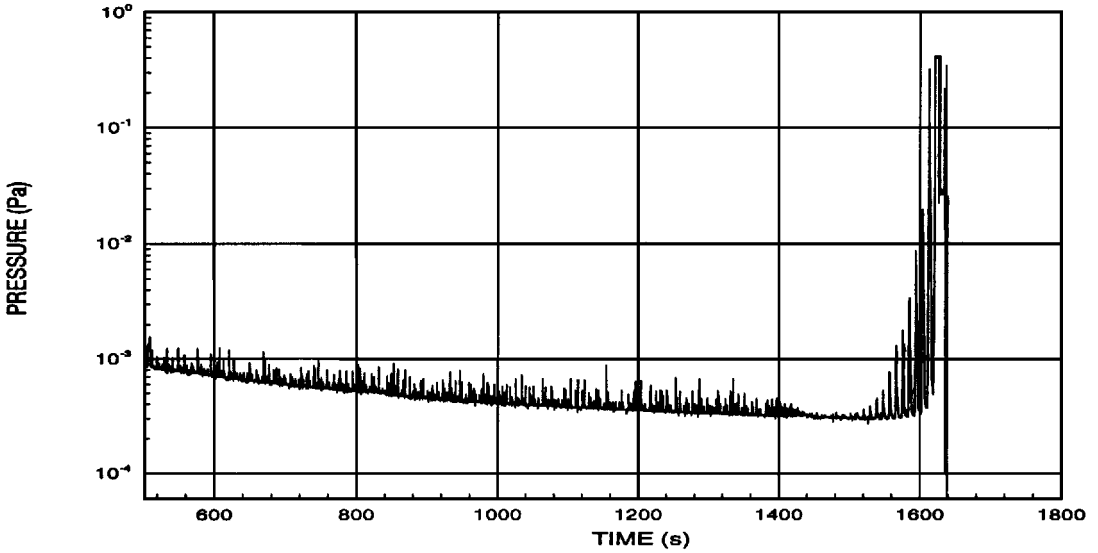


Fig. 5 Pressure measurements during the entire EMP flight.

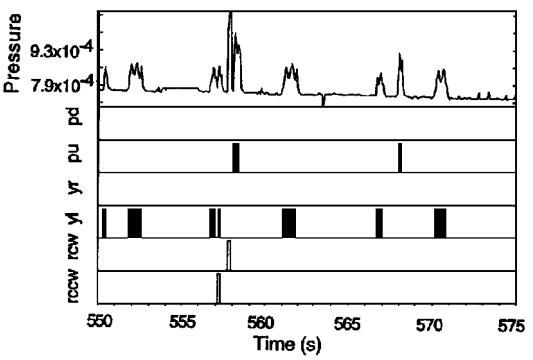


Fig. 6 Pressure measurements during the EMP thruster-firing period.

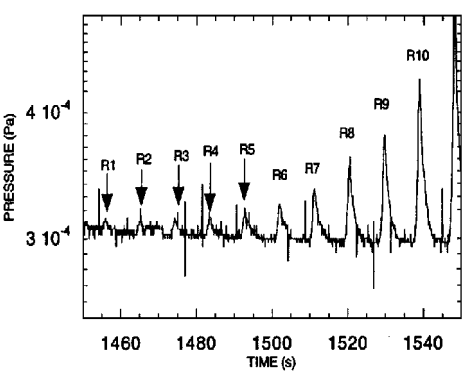


a) Pressure pulses $R_1$ to $R_{10}$

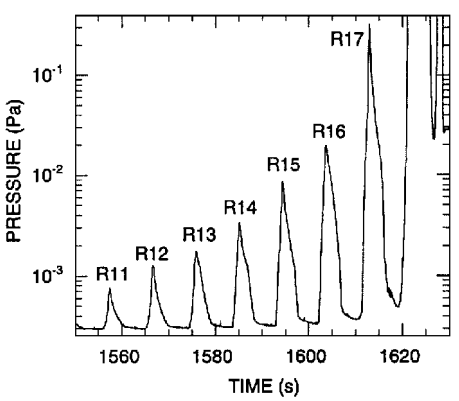


b) Pressure pulses $R_{11}$ to $R_{17}$

Fig. 7 Pressure measurement during the EMP ram-wake period.

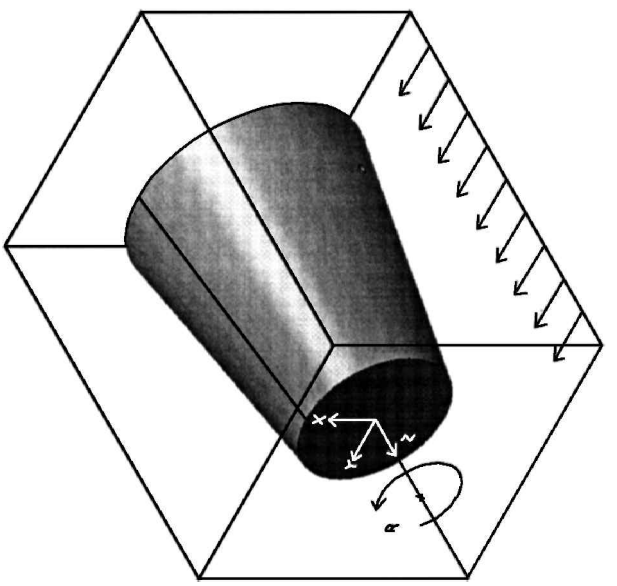

Fig. 8 EMP geometry showing the incoming freestream, the direction of EMP rotation, and the entrance of the pressure tube.

$Z$ so that the $Y$ axis is parallel to the centerline of the pressure tube. The orientation of the tube during a complete spacecraft revolution is examined, as shown in Fig. 9. The angle $o$ between the freestream velocity vector and the $Y$ axis is measured counterclockwise from the freestream direction. The angle $\theta$ measures the polar position of the entrance of the tube and is measured counterclockwise from the freestream. At position (A), the tube is facing the wake of the spacecraft with $o = 180$ deg and $\theta = 155$ deg. At position (E) the tube is facing the ram direction with $o = 360$ deg and $\theta = 335$ deg. The sequence of the tube positions during a complete revolution is shown in Fig. 9 at intervals of $\Delta\theta = 45$ deg or every 1.027 s.

The details of a typical pressure pulse and the sequences as previously discussed are shown in Fig. 10 for revolutions $R_{16}$ and $R_{17}$. One of the most distinct characteristics of the pressure pulses is their asymmetry with respect to their peak value, as can be seen in Fig. 10. The pressure rises sharply between positions (B) and (E) and then falls gradually until the tube reaches position (I). The asymmetry is a result of both the placement of the tube at the off-axis location, as well as the polar location of the tube entrance during the revolution. In the case of a constant incoming freestream, a tube aligned with the radial direction would have recorded a symmetrical pressure distribution.

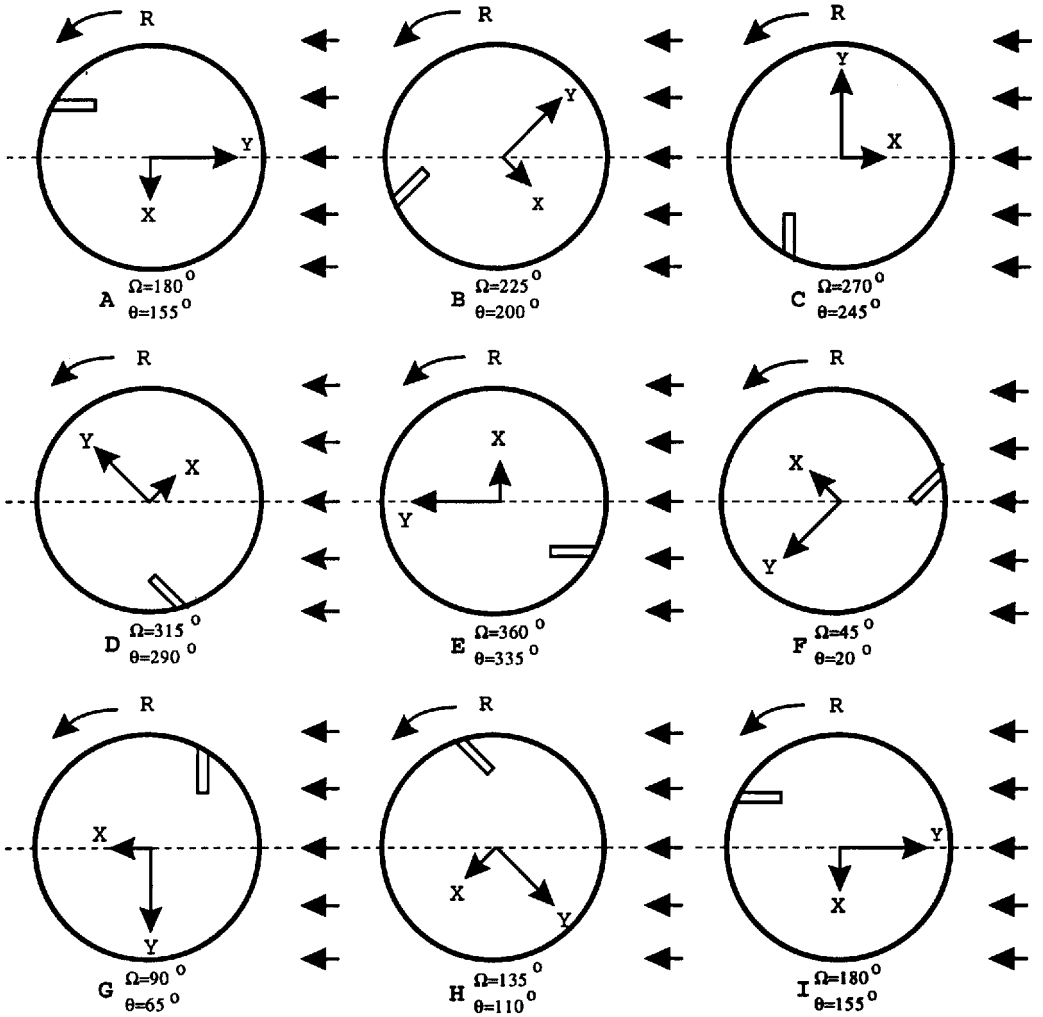


**Fig. 9 Pressure-sensor plane showing the pressure tube position at intervals of 1.025 s during an EMP revolution (looking aft). The polar angle of the tube entrance is $\theta$ and the angle between ram and $Y$ axis is $\Omega$.**

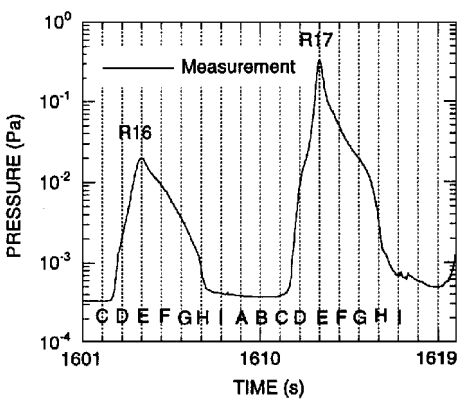


**Fig. 10 Details of pressure measurements during EMP revolutions $R_{16}$ and $R_{17}$.**

## DSMC Results and Analysis

The analysis and simulation of the EMP pressure sensor must account for both the external and internal flowfields. Note that the gas system inside the pressure apparatus was not static and, as a result, the measurements do not correspond to the usual Maxwellian pressure. The characteristics of the flowing gas are important and, as such, the sensor most likely measured the arrival rate of molecules. Therefore, steady state does not represent an equilibrium condition but rather the steady rate of arrival of molecules in the pressure chamber. There are several contributions to the flux and, subsequently, the pressure in the chamber. First, there is a contribution due to the outgassing of the gauge itself. The outgassing history has been measured, and it was found that the most significant constituent was water vapor. The second contribution is the net flux into the sensor chamber due to the molecules entering or leaving through the tube. This flux includes molecules that arrive in the chamber without experiencing any collisions with the surfaces of the tube, as well as those that experience such collisions. It also includes molecules that leave the chamber and escape through the tube. In the case of free-molecular flow conditions, this problem has similarities with the classic one analyzed by many investigators as referenced in the Introduction. This flux depends, among other parameters, on the length-to-tube ratio, the degree of rarefaction of the flow, the temperature of the surfaces, and the nature of surface interactions, as well as the dimensions of the pressure chamber itself. In the absence of ionization, the pressure in a large chamber would reach a value so that the incoming and outgoing fluxes are at equilibrium. However, in the cold cathode sensor, the molecules inside the pressure chamber become ionized and the sensor acts as a sink of the arriving molecules.

### External-Flowfield Computations

A series of simulations is conducted first to analyze the external flowfield around the EMP and investigate specifically the pressure-sensor entry region during the ram-wake period. A three-dimensional version of the DSMC program F3 developed by Bird[9] is used for the simulations. The altitudes of interest during the ram-wake period were above 130 km and the ambient mean-free paths larger than 9 m. As a result, the EMP was in the near- to free-molecular flow regimes during this part of the mission. The revolution $R_{17}$ is analyzed first and DSMC simulations are performed for tube positions $R_{17A}$ to $R_{17I}$ as described in Fig. 9. At $R_{17A}$ the EMP was at an altitude of 154.2 km with the tube facing the wake. At $R_{17I}$ the EMP was at an altitude of 129.5 km with the tube facing the wake

**Table 1 Freestream conditions for the EMP revolution $R_{17}$**

| Position | Altitude, km | Number density, $m^{-3}$ | Mass density, $kg/m^3$ | $T_\infty$, K | Mole fraction N | $N_2$ | O | $O_2$ | He | $V_\infty$, m/s | $\lambda_\infty$, m |
|---|---|---|---|---|---|---|---|---|---|---|---|
| A | 154.2 | $4.83 \times 10^{16}$ | $1.507 \times 10^{-9}$ | 711 | 0.000424 | 0.553 | 0.400 | 0.0453 | 0.000579 | 6505 | 41 |
| B | 151.2 | $5.52 \times 10^{16}$ | $1.723 \times 10^{-9}$ | 711 | 0.000320 | 0.566 | 0.386 | 0.0472 | 0.000523 | 6509 | 36 |
| C | 148.1 | $6.36 \times 10^{16}$ | $1.985 \times 10^{-9}$ | 711 | 0.000236 | 0.578 | 0.372 | 0.0492 | 0.000470 | 6514 | 31 |
| D | 145.0 | $7.39 \times 10^{16}$ | $2.306 \times 10^{-9}$ | 675 | 0.000170 | 0.591 | 0.357 | 0.0514 | 0.000418 | 6518 | 26 |
| E | 141.9 | $8.66 \times 10^{16}$ | $2.705 \times 10^{-9}$ | 675 | 0.000120 | 0.604 | 0.342 | 0.0539 | 0.000368 | 6522 | 22 |
| F | 138.8 | $1.03 \times 10^{17}$ | $3.208 \times 10^{-9}$ | 633 | 0.000082 | 0.616 | 0.327 | 0.0566 | 0.000319 | 6527 | 19 |
| G | 135.7 | $1.23 \times 10^{17}$ | $3.885 \times 10^{-9}$ | 583 | 0.000055 | 0.629 | 0.310 | 0.0598 | 0.000270 | 6531 | 15 |
| H | 132.6 | $1.51 \times 10^{17}$ | $4.708 \times 10^{-9}$ | 583 | 0.000035 | 0.643 | 0.294 | 0.0634 | 0.000222 | 6536 | 13 |
| I | 129.5 | $1.88 \times 10^{17}$ | $5.861 \times 10^{-9}$ | 526 | 0.000022 | 0.656 | 0.276 | 0.0678 | 0.000176 | 6540 | 10 |

after having completed a full rotation. Each simulation is run until steady state, usually achieved within milliseconds. The changes of the freestream conditions in 1 ms can be considered insignificant because the altitude change is less than 70 m and the angle of rotation of the tube is 0.4 deg. The freestream parameters used in the simulations are shown in Table 1. Six species ($N_2$, $O_2$, N, O, NO, and He) and a chemical reaction model suitable for reentry conditions are included. The freestream data for $N_2$, $O_2$, N, O, and He are taken from the MSIS[10] model because no in-situ measurements are available from the EMP mission. No ionic species are included in the simulations because neutrals dominate the ambient composition at the altitudes considered.

The computational region in each simulation is large enough that it retains the undisturbed freestream conditions at the boundaries away from the body. The freestream velocity vector is in the $Y$ direction, and the long side of the EMP is aligned with the $Z$ axis. The simulations utilize a maximum of 700,000 particles and 8000 cells. Of those cells, 1000 are located near the surface of the body and approximately 500 are surface cells. The size of subcells is 0.03 m and that of the pixels used for the geometric definition of the body is 0.0125 m. The size of cells and subcells is based on the local mean-free path, which is expected to decrease in the density enhancement ahead of the body. Diffuse reflection is assumed with complete accommodation on the surface. The temperature of the external surfaces is taken to be 300 K, based on measurements taken on the EMP spacecraft.

The general characteristics of the external flowfield are discussed first for the $R_{17E}$ simulation. The flowfield structure for the density and the overall temperature are shown in Fig. 11. The density shown in Fig. 11a for a plane $X = 0$ exhibits the development of an enhancement region with a maximum of 19 times the freestream value. The region of this diffuse shock wave extends over a large distance ahead of the body as expected in an almost free-molecular flow.[3] The asymmetry in the flowfield is caused by the angle of the surface with the freestream. The density at the pressure-sensor plane is shown in Fig. 11b. The wake shows values below 0.05, although more detailed simulations are needed to describe this highly rarefied region accurately. The overall temperature is shown in Figs. 11c and 11d. The temperature rises at almost 12 times the freestream value, and the disturbance extends much larger distances than that of the density disturbance. The temperature distribution is also asymmetric with respect to the $Y$ axis and shows increased values in the wake, which is a region of extreme nonequilibrium.

The effects of species separation also need to be considered. Figure 12 shows the distribution of the number fraction of $N_2$ and O. The observed variations compared with the freestream values are the result of thermal and pressure diffusion. The concentration of the relatively heavier species $N_2$ is shown to increase close to the body. In contrast, the lighter O shows an increase ahead of the diffuse shock and a decrease close to the body. These effects are the opposite in the wake region of the spacecraft. It is expected, therefore, that the composition of the flux entering the pressure tube will depend on the polar angle of the tube entrance.

The normalized density and temperatures along a streamline at the plane of the pressure sensor are shown in Fig. 13. There is a significant degree of nonequilibrium, as indicated by this figure. The rotational and vibrational temperatures remain close to the undisturbed value as a result of few collisions that could excite the internal

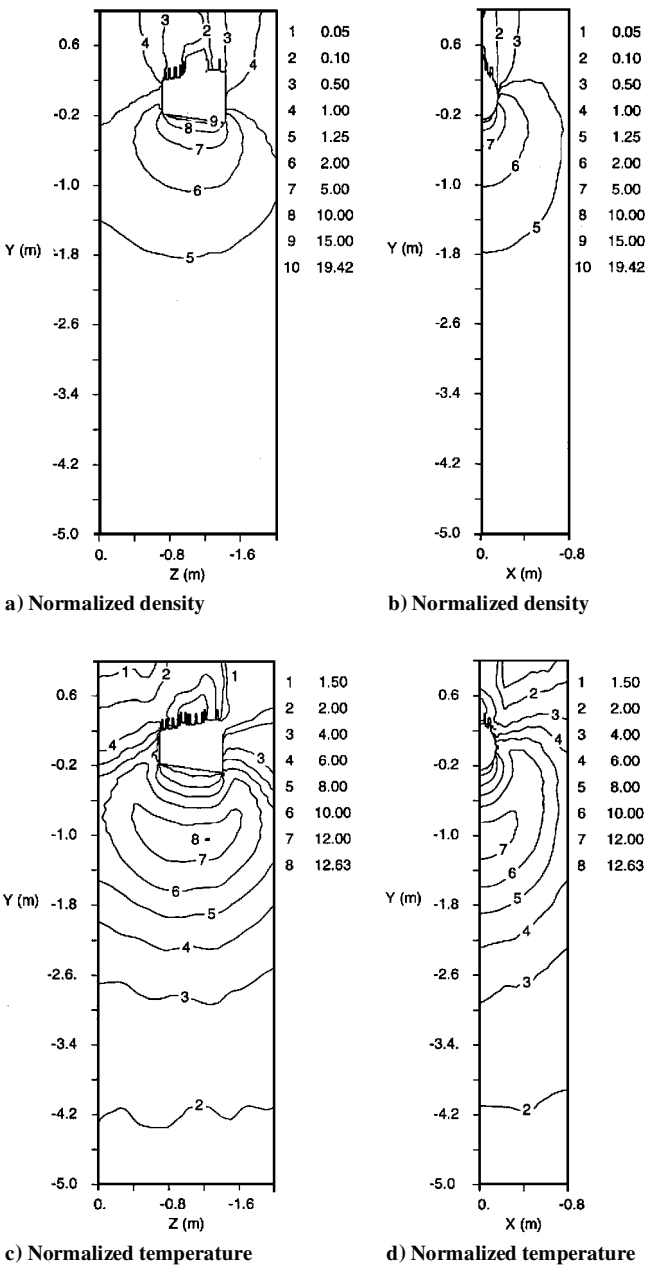


**a) Normalized density** **b) Normalized density**

**c) Normalized temperature** **d) Normalized temperature**

**Fig. 11 Normalized density and temperature at the $X = 0$ plane (left) and pressure-sensor plane (right, looking forward) for $R_{17E}$.**

degrees of freedom. The translational temperature rises to almost 12 times the freestream value, not as a result of collisions but because of the superposition of the incoming and reflected distributions off the surface.[11] As previously explained, the region of thermal disturbance extends well ahead of the density disturbance. Figure 14 shows the species composition along a stagnation line at the plane of the sensor. The species concentrations remain almost constant in front

**Table 2 Freestream conditions for pressure peaks $R_{12}-R_{16}$**

| Pressure peak | Altitude, km | Number density, $m^{-3}$ | Mass density, $kg/m^3$ | $T_\infty$, K | Mole fraction N | $N_2$ | O | $O_2$ | He | $V_\infty$, m/s | $\lambda_\infty$, m |
|---|---|---|---|---|---|---|---|---|---|---|---|
| $R_{15E}$ | 196.8 | $1.14 \times 10^{16}$ | $3.59 \times 10^{-10}$ | 886 | 0.00399 | 0.39304 | 0.57569 | 0.02554 | 0.00173 | 6444 | 179 |
| $R_{14E}$ | 223.6 | $5.41 \times 10^{15}$ | $1.69 \times 10^{-10}$ | 922 | 0.00679 | 0.29796 | 0.67531 | 0.01682 | 0.00311 | 6405 | 384 |
| $R_{13E}$ | 249.6 | $3.03 \times 10^{15}$ | $9.48 \times 10^{-11}$ | 936 | 0.00842 | 0.22937 | 0.74581 | 0.01151 | 0.00489 | 6368 | 687 |
| $R_{12E}$ | 275.0 | $1.77 \times 10^{15}$ | $5.54 \times 10^{-11}$ | 943 | 0.00951 | 0.17336 | 0.80197 | 0.00775 | 0.00742 | 6332 | 1177 |

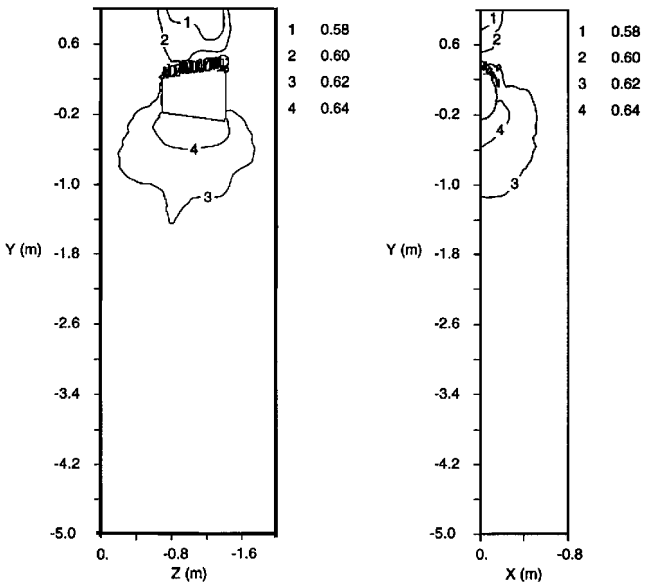


a) $N_2$ mole fraction b) $N_2$ mole fraction

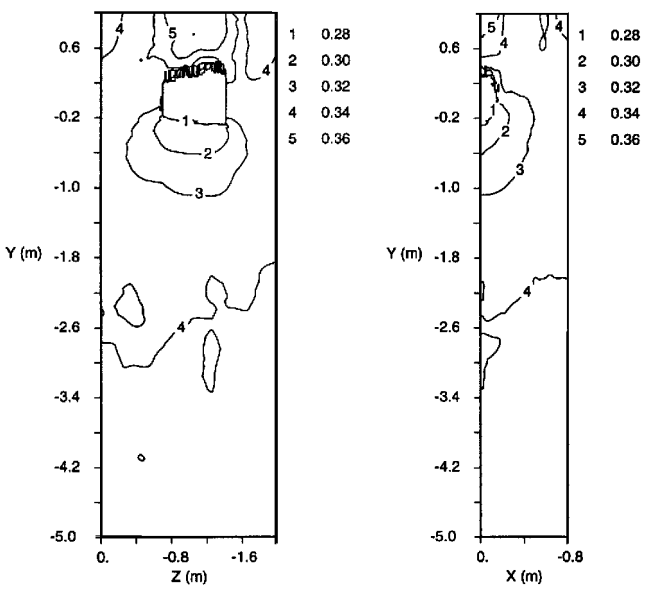


c) O mole fraction d) O mole fraction

**Fig. 12 Species composition at the $X = 0$ plane (left) and the pressure-sensor plane (right, looking forward) for $R_{17E}$.**

of the spacecraft and close to their freestream values, indicating that there is very little chemical activity in the gas. The small variations are the result of thermal and pressure diffusion, as explained before.

The simulation $R_{17}$ is chosen as the lower boundary of the mission envelope. It is evident that at higher altitudes the flow will be entirely in free-molecular regime with important implications for the pressure measurements. As explained before, the pressure-sensor measurements relate to the incident pressure at the entrance of the tube. To obtain the incident pressure during the complete revolution $R_{17}$, a series of simulations are performed with freestream conditions, as shown in Table 1. Additional computations are performed with freestream conditions appropriate to those of the pressure peaks between $R_{12}$ and $R_{16}$ as described in Tables 2 and 3. In Fig. 15, the

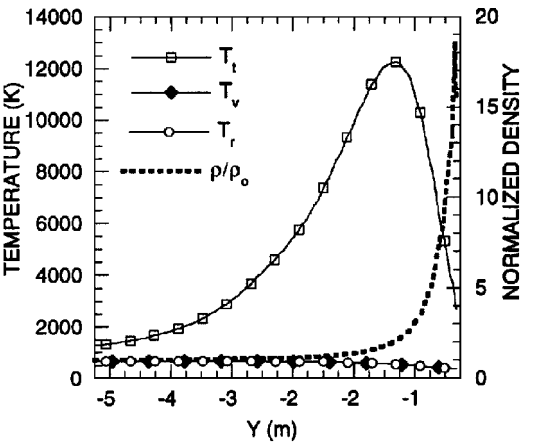


**Fig. 13 Flowfield properties on a streamline at the pressure-sensor plane for $R_{17E}$.**

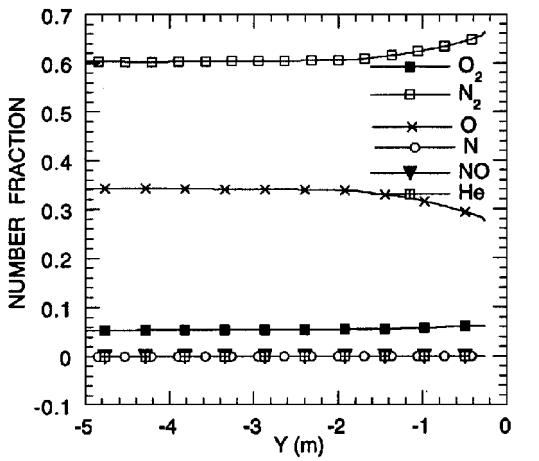


**Fig. 14 Chemical composition along a streamline at the pressure-sensor plane for $R_{17E}$.**

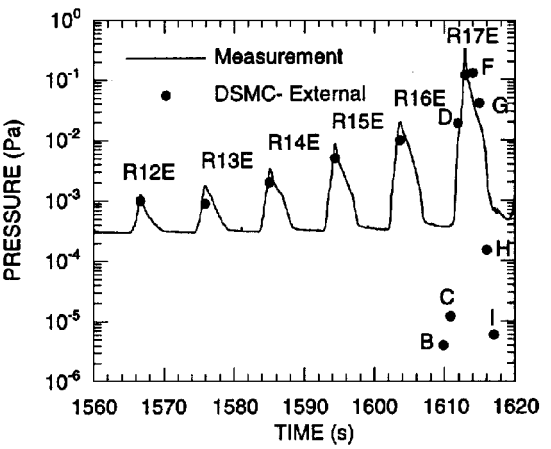


**Fig. 15 Comparison between the DSMC external incident pressure at the location of the pressure tube entrance (symbols) and measured pressure (line).**

**Table 3 Freestream conditions during EMP revolution $R_{16}$**

| Pressure peak | Altitude, km | Number density, $m^{-3}$ | Mass density, $kg/m^3$ | $T_\infty$, K | Mole fraction N | $N_2$ | O | $O_2$ | He | $V_\infty$, m/s | $\lambda_\infty$, m |
|---|---|---|---|---|---|---|---|---|---|---|---|
| $R_{16D}$ | 172.5 | $2.38 \times 10^{16}$ | $8.84 \times 10^{-10}$ | 825 | 0.00157 | 0.4810 | 0.4810 | 0.03533 | 0.00099 | 6479 | 85 |
| $R_{16E}$ | 169.5 | $2.64 \times 10^{16}$ | $9.86 \times 10^{-10}$ | 814 | 0.00133 | 0.4923 | 0.4688 | 0.03675 | 0.00091 | 6482 | 77 |
| $R_{16F}$ | 166.5 | $2.95 \times 10^{16}$ | $1.11 \times 10^{-9}$ | 801 | 0.00109 | 0.5041 | 0.4556 | 0.03830 | 0.00084 | 6487 | 68 |

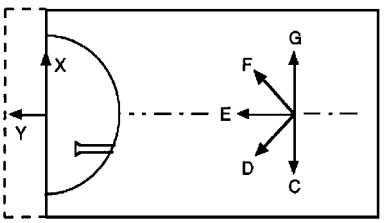


**Fig. 16 DSMC domain used for the internal EMP calculations. The direction of the freestream is shown at various points during the EMP revolution.**

incident pressure at the location of the tube entrance is plotted as a function of time along with the measured pressure inside the sensor. The reflected pressure was found to be very small in comparison to the incident pressure because of the diffuse nature of the surface interaction. The incident pressure, therefore, would be the pressure measured by a sensor located at the surface of the EMP. The DSMC external pressure shows the rise from (C) to (D) and it is asymmetric. The pressure at position (E) is underpredicted whereas at position (F) is overpredicted. It is clear from Fig. 15 that the shape of the measured pressure pulse is not in good qualitative agreement with the DSMC external pressure. The predicted asymmetry clearly shown in Fig. 15 between positions (D) and (G) is a direct result of the position of the entrance of the pressure tube and the increased altitude. As Fig. 9 shows at position (D), the tube has a $\theta = 290$ deg, whereas at (F), it has a $\theta = 20$ deg, and the DSMC external incident pressure clearly demonstrates that effect. However, unlike the measurements, the DSMC external pressure between positions (E) and (F) is comparable because the tube entrance is at almost equal angles from the freestream vector. It is concluded that the external flow is not sufficient to explain the measured pressure pulse because the analysis does not include the tube and pressure chamber effects.

#### Internal/External Flowfield Computations

A series of three-dimensional DSMC computations are performed next to investigate the flowfield inside the pressure apparatus during the spacecraft revolution. The external flow simulations clearly indicated the three-dimensional character of the flow at the tube entry region. To address the coupling between the external and internal flows, the computational region includes the pressure apparatus and is extended almost 1 m ahead of the EMP, as shown in Fig. 16. Only half of the EMP spacecraft is used, and the simulation region includes the 0.1-m length, 0.022-m-diam tube attached to the pressure-sensor chamber with a 0.02-m length and 0.03-m end diameter. The detailed geometry with the dimensions used in the DSMC simulations is shown in Fig. 4. The subcell and pixel sizes are 0.011 m and $2.75 \times 10^{-3}$ m, respectively, smaller than the external flow simulations, to achieve adequate discretization inside the tube and pressure apparatus. The volume is discretized using 8500 cells and a maximum of 700,000 particles. The freestream conditions used in these simulations correspond to EMP positions $R_{16D}$, $R_{16E}$, $R_{16F}$, and $R_{17C}$, $R_{17D}$, $R_{17E}$, $R_{17F}$, $R_{17G}$, as shown in Fig. 9. The freestream conditions are shown in Tables 1 and 3. Each DSMC simulation—corresponding to a specific tube location during the EMP revolution—is run until steady state, which is achieved within milliseconds. As explained previously, during 1 ms the EMP rotated for about 0.4 deg and lost approximately 70 m in altitude. These changes in angle of attack, altitude, and freestream parameters are considered negligible, and it is assumed that the flow reaches equilibrium in the tube-chamber system during each DSMC computation.

The density and temperature distributions in Fig. 17, for clarity, show only a small portion of the computational domain. Three tube positions during the EMP revolution $R_{17}$ are shown with $\Omega = 315$, 360, and 45 deg, respectively. These conditions correspond to (D), (E), and (F) EMP positions, as shown in Fig. 9.

At position $R_{17D}$, the tube has an $\Omega = 315$ deg and faces the flow at an angle of attack of $-45$ deg. The density increases from its freestream value and reaches a maximum of approximately $20n_\infty$ at one tube diameter $D_t$ from the entrance. The density then decreases monotonically until the pressure chamber. The flow structure is three-dimensional at the tube entry region and becomes axisymmetric after a distance of two tube diameters downstream of the entrance. The temperature shown in Fig. 17 (top) decreases from the entrance of the tube and reaches a value of $0.5T_\infty$, equal to the tube wall temperature of $T_t = 300$ K. These results show that the gas reaches an equilibrium with the walls at a distance of two tube diameters.

At position (E), the tube has $\Omega = 360$ deg and is facing the incoming flow directly. The density and temperature distributions are shown in Fig. 17 (middle). The density increases monotonically from its freestream value to a value of $15n_\infty$ at the entrance of the tube and reaches a maximum of $30n_\infty$ within the pressure chamber. This value is equivalent to the external surface density maximum as discussed in the previous section. The temperature distribution is axisymmetric for the entire length of the tube and reaches wall equilibrium only within the pressure chamber.

At position (F), the tube has $\Omega = 45$ deg and faces the flow at an angle of attack of 45 deg. The density increases from its freestream value and reaches a maximum of $30n_\infty$ at approximately one tube diameter downstream of the entrance, as Fig. 17 (bottom) shows. The density decreases from the maximum monotonically up to the pressure chamber. The density exhibits three-dimensional effects up to almost $2D_t$ from the entrance and then becomes axisymmetric. The temperature, shown in Fig. 17, comes into an equilibrium with the wall at a distance of two diameters.

Although the angle of attack with respect to the tube axis is $\pm 45$ deg in (D) and (F), respectively, there are large differences in the flow structures between these two cases. These differences are entirely due to the three-dimensional character of the external flow at the tube entry region. Because of the asymmetric position of the tube with respect to the external EMP surface, the tube and the pressure chamber are exposed in case (F) to a larger incoming flux than in case (D). As a result, both the maximum tube density and the chamber density are higher in case (F). Temperature equilibration also is delayed by almost a half a tube diameter in (F), but generally, the temperature remains in wall equilibrium. Although the flow and geometric parameters were different, our results are similar to those of Moss and Bird.[8] Using a tube of $L_t = 8.7$ cm and $D_t = 0.235$ cm at 29 deg with the freestream, they predicted that the flow becomes axisymmetric in two to three diameters from the entry point. Similarly, the density in their simulations increased from the external flow and reached a maximum inside the tube. Temperature also was decreasing from the entrance and reached wall equilibrium at a distance of a few diameters downstream of the entrance.

In the ram case, while the EMP is at position (E) the direct incoming flux penetrates the tube all the way to the chamber. Unlike cases (D) and (F), the density increases monotonically from the freestream and reaches a maximum at the end of the chamber. The temperature also reaches wall equilibrium only within the pressure chamber, where there are sufficient collisions with its walls.

The surface pressure for all three simulations evaluated at various locations in the tube and chamber is shown in Fig. 18. The ram case $R_{17E}$ shows that the pressure remains almost constant at $10^{-2}$ Pa, reaching a maximum at the end of the pressure chamber of $2.9 \times 10^{-2}$ Pa. This pressure is close to the semianalytical prediction of $5.7 \times 10^{-2}$ Pa based on the theory of Hughes and de Leeuw.[5] This theory was developed assuming that the flow in the large reservoir at

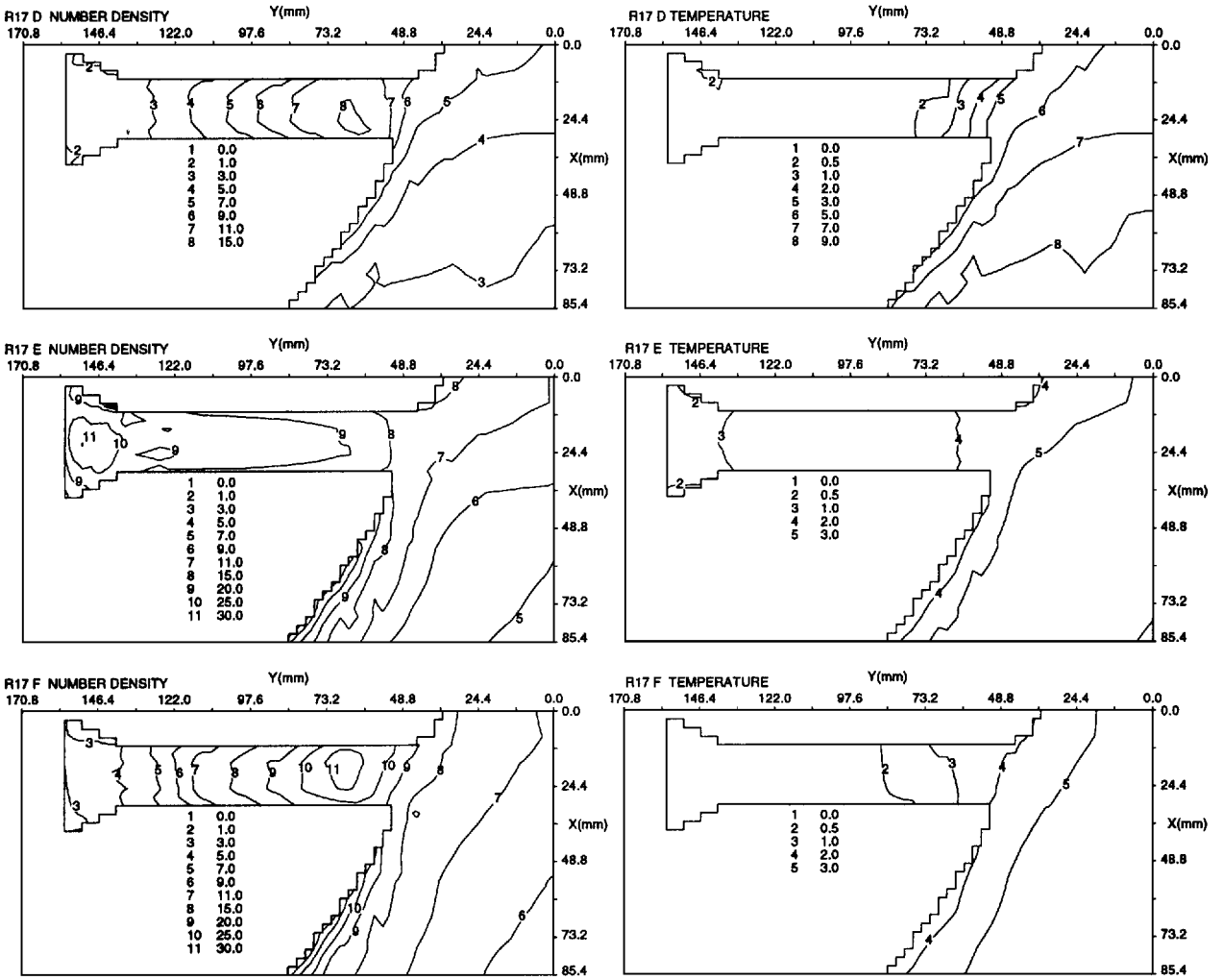


**Fig. 17 Detailed view of normalized density and temperature for three positions during the EMP revolution $R_{17}$: top) $R_{17D}$, $\Omega = 290$ deg; middle) $R_{17E}$, $\Omega = 360$ deg; and bottom) $R_{17F}$, $\Omega = 45$ deg.**

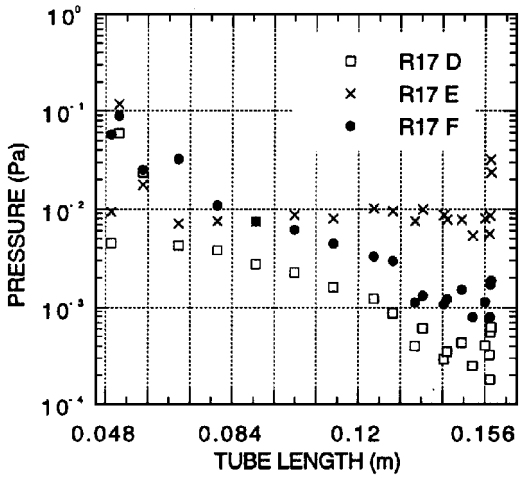


**Fig. 18 Surface pressure inside the pressure sensor tube and chamber for three positions during the EMP revolution $R_{17}$.**

the end of the tube is at equilibrium. The agreement between DSMC and theory suggests that, despite the small size of the EMP pressure chamber, the flow inside is in equilibrium with the walls. The surface pressure as shown in Fig. 18 decreases with distance from the tube entrance for $R_{17D}$ and $R_{17F}$. In both cases, the effects of angle of attack and EMP surface modify the internal flow. The average tube surface pressure for $R_{17F}$ is shown in Fig. 18 to be higher than the average pressure of $R_{17D}$ case. Also, the surface pressure at the end of the chamber is approximately $3 \times 10^{-4}$ Pa for the $R_{17D}$ and $10^{-3}$ Pa for the $R_{17F}$ case. The Hughes and de Leeuw predictions for cases $R_{17D}$ and $R_{17F}$ are $8.2 \times 10^{-3}$ and $1.1 \times 10^{-2}$ Pa, respectively. The difference between the two theoretical values is due to the change in freestream density and temperature. The differences between the theoretical and DSMC results for (D) and (F) can be attributed to the effects on the internal flow caused by the EMP surface. These external geometric effects are not included in the Hughes and de Leeuw theory.

A plot of the predicted average surface pressure at the end of the chamber is shown in Fig. 19 in comparison with the measured pressure for a complete revolution $R_{17}$ and selected points during the $R_{16}$ revolution. The external surface pressure at the location of the tube entrance also is shown for comparison. It is clear that the DSMC internal simulations predict qualitatively the asymmetric pressure pulse measured during the EMP revolution. A sharp increase from (D) to (E) and a gradual fall to (F) are clearly demonstrated in Fig. 19 for both revolutions. However, the magnitudes of the pressure are much smaller than the measurements although the simulations assumed a closed chamber pressure at the end, a situation that would predict the maximum surface pressure. The most important factor that contributes to the underprediction of the pressure pulse by the DSMC is the absence of in-situ knowledge of the EMP freestream data. In the simulations the freestream number density and composition are based on MSIS, a regression model for the spatially and time-varying thermosphere. Because the exact mission profile of the EMP is not known, many of the inputs to the MSIS model are approximate. As can be seen from Fig. 19, the $R_{17E}$ DSMC prediction using $n_\infty = 8 \times 10^{16}$ m$^{-3}$ matches closely the $R_{16E}$ measurement. Note that the $R_{16E}$ simulation using a value of

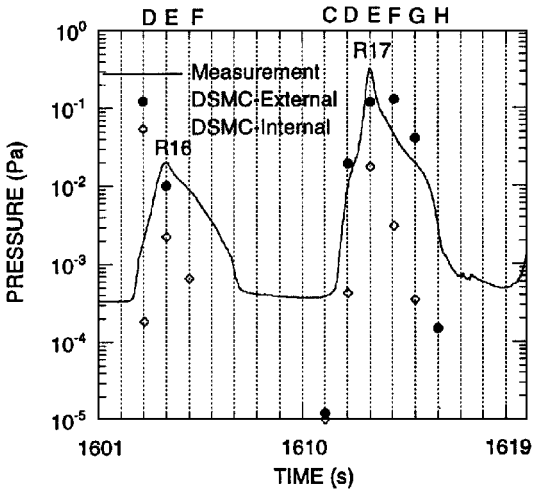


**Fig. 19 Comparison between measured pressure, the DSMC external incident pressure at the tube entrance, and DSMC chamber pressure for $R_{16}$ and $R_{17}$.**

$n_\infty = 2.64 \times 10^{16}$ m$^{-3}$ underpredicts the $R_{16E}$ measurement. The DSMC internal predictions for the ram cases $R_{12E}-R_{17E}$ also have been found to match those predicted by the Hughes and de Leeuw theory. Because the EMP geometry has minimal effects on the internal pressure for the zero angle-of-attack cases $R_{12E}-R_{17E}$, the theoretical predictions can be used to validate the DSMC results. In addition, Figs. 15 and 19 show that the external DSMC pressures for the ram cases $R_{12E}-R_{17E}$ are lower than the internal measurements. All of the above arguments suggest that the underprediction can be attributed to the use in the simulations of freestream number density values that are lower than the actual ones. Therefore, given the uncertainty in the freestream data, the underprediction of the magnitude of the pressure is not of concern. What is more important, as Fig. 19 shows, the DSMC simulations predict the shape of the pressure pulse very well and demonstrate the importance of coupling between external and internal flows, as well as the effect of the spacecraft and instrument geometry on the pressure measurements.

Another factor that may contribute to the enhanced pressure levels in the chamber is the outgassing in the tube and pressure chamber. External outgassing also may contribute partly to the incoming flux. It is expected, however, that this component is smaller than the internal one because the outgassed molecules have a velocity component away from the spacecraft. The effects of the outgassing on the pressure are shown in Fig. 5 and are not included in the DSMC simulations.

## Conclusions

The DSMC method was utilized to investigate the response of a pressure apparatus in the near- to free-molecular flow regimes. The DSMC results were compared with data obtained during a flight experiment designed to measure the induced environment about the EMP suborbital vehicle. During the quiet thruster period from 560 km and until reentry at 130 km, asymmetric pressure pulses due to ram-wake effects were recorded. The pressure data were recorded with a pressure sensor that was connected with a tube to the surface of the rotating spacecraft.

The external flowfield about the EMP spacecraft was simulated using a three-dimensional DSMC code. The density, temperature, and species composition distributions exhibited three-dimensional and nonequilibrium effects consistent with previous simulations at similar altitudes. The flux and composition at the pressure-tube entry region were found to depend on the location of the tube during the EMP revolution. The DSMC predictions of the pressure incident to the tube entrance were compared with data. It was concluded that the external flow alone is not capable of explaining the observations and that the internal flow affected the measurements as well.

Additional three-dimensional DSMC computations that included the pressure apparatus were performed. The internal flow is influenced by the three-dimensional character of the external flow at the tube entrance. The entry flow region is affected by the spacecraft geometry, as well as the asymmetric location of the tube with respect to the EMP surface. The flow in the simulations reached equilibrium with the wall at locations downstream of the tube entrance depended upon the angle of attack. It was found that, in the case of zero angle of attack, the flow reached equilibrium only within the pressure chamber. The surface pressure in the tube and chamber also was found to depend on the angle of attack.

For the cases of nonzero angle of attack, the pressure decreased with distance from the tube entrance but remained almost constant for the zero angle-of-attack case. The surface pressure pulse at the end of the chamber predicted by the DSMC was found to be in good qualitative agreement with measurements. Differences in the magnitude are attributed primarily to the lack of knowledge of the actual freestream conditions. Another contributing factor to the underprediction may be due to the absence from the simulations of the internal outgassing of the pressure apparatus.

This study demonstrated that the rarefied flow into the tube and chamber of the pressure apparatus onboard the EMP suborbital vehicle exhibited nonequilibrium and three-dimensional effects. The pressure measured inside the sensor was affected by the geometry of the vehicle and the connecting tube, as well the ambient and induced freestream conditions. Flow conditions and composition inside the pressure chamber were different from the ambient undisturbed parameters. These conclusions can be applied to other environmental measurements obtained with instruments housed inside a spacecraft and connected to the outside through an opening or a tube. In such cases, the data obtained must be interpreted carefully. An important tool in the analysis and interpretation is the DSMC method, which can be used very effectively for both pre- and postflight predictive purposes.

## Acknowledgments

Partial support for N. A. Gatsonis and R. E. Erlandson was provided by the Vehicle Interactions Program at the Johns Hopkins University Applied Physics Laboratory and for N. A. Gatsonis and E. P. Maynard by the JHU/APL Subcontract 606193-0. The authors would like to thank Simon Wing for assistance in data analysis, K. Kumar, S. Swaminathan, and D. Rault for useful discussions, and G. Bird for providing a version of his F3 programs.

## References

[1]Bird, G. A., *Molecular Gas Dynamics and the Direct Simulation of Gas Flows*, Oxford Univ. Press, Oxford, England, UK, 1994.

[2]Moss, J. N., and Bird, G. A., "Direct Simulations of Transitional Flow for Hypersonic ReEntry Conditions," *Thermal Design of Aeroassisted Orbital Transfer Vehicles*, edited by H. F. Nelson, Vol. 96, Progress in Astronautics and Aeronautics, AIAA, New York, 1985, pp. 113–139.

[3]Dogra, V. K., Wilmoth, R. G., and Moss, J. N., "Aerothermodynamics of a 1.6-Meter Diameter Sphere in Hypersonic Rarefied Flow," *AIAA Journal*, Vol. 30, No. 7, 1992, pp. 1789–1794.

[4]Rault, D. F., "Aerodynamic Characteristics of a Hypersonic Viscous Optimized Waverider at High Altitudes," *Journal of Spacecraft and Rockets*, Vol. 31, No. 5, 1994, pp. 719–727

[5]Hughes, P. C., and de Leeuw, J. H., "Theory for the Free Molecule Impact Probe at an Angle of Attack," *Rarefied Gas Dynamics*, Vol. 1, Academic, New York, 1965, pp. 653–676.

[6]Fan, C., and Robertson, S. J., "Monte Carlo Solutions of Mass, Momentum and Energy Transfer for Free Molecule and Near-Free Molecule Flow Through Circular Tubes," *Proceedings of the 6th International Symposium on Rarefied Gas Dynamics*, edited by L. Trilling and H. Wachman, 1969, pp. 655–666.

[7]Kannenberg, K. C., and Boyd, I. D., "Monte Carlo Computation of Rarefied Supersonic Flow into a Pitot Probe," *AIAA Journal*, Vol. 34, No. 1, 1996, pp. 83–88.

[8]Moss, J. N., and Bird, G. A., "Monte Carlo Simulations in Support of the Shuttle Upper Atmospheric Mass Spectrometer Experiment," *Journal of Thermophysics*, Vol. 2, No. 2, 1988, pp. 138–144.

[9]Bird, G. A., *The F3 Program System Users Manual*, Ver. 1.0, Jan. 1991.

[10]Hedin, A. E., "MSIS-86 Thermospheric Model," *Journal of Geophysical Research*, Vol. 92, No. 5, 1987, pp. 4649–4662.

[11]Wilmoth, R. G., Dogra, V. K., and Moss, J. N., "Energetics of Gas-Surface Interactions in Transitional Flows at Entry Velocities," *Journal of Spacecraft and Rockets*, Vol. 29, No. 6, 1992, pp. 786–793.

I. D. Boyd
*Associate Editor*